Lasers in Manufacturing and Materials Processing
https://doi.org/10.1007/s40516-024-00251-y

RESEARCH

Evaluating the Effect of Deposition Strategy on Mechanical Characteristics of 316L Parts Produced by Laser Powder Directed Energy Deposition Process

Gabriele Piscopo[1] · **Luca Iuliano**[1]

Accepted: 13 March 2024

Abstract

The production of large components, the possibility to repair damaged parts and the ability to produce components of multi-graded or functional-graded materials are the main drivers of the research and the application of the Laser Powder Directed Energy Deposition (LP-DED) process. However, the knowledge of the process and of the relationships among the process parameters and the characteristics of the produced part is currently not completely understood. The aim of this paper is to fill the current gap in the scientific literature related to the effect of the deposition strategy on the part quality. Therefore, the influence of two of the most important parameters, namely the deposition path and the idle time, on the residual stresses and porosity is evaluated on 316L samples produced by the LP-DED process. The obtained results show that both parameters have a high influence on the porosity level and the residual stresses. In particular, it can be seen that a high value of idle time worsens both porosity and residual stresses. Then, it is also observed that the raster deposition path leads to a lower value of stresses.

Keywords Additive manufacturing · Directed Energy Deposition · AISI 316L · Deposition strategy

Introduction

Additive Manufacturing (AM) processes have opened new opportunities in manufacturing industries in terms of part design and production methods [1]. Due to the enormous advantages of AM with respect to conventional processes, it is one of the most growing technologies [2]. As a result, several sectors are introducing AM processes into their manufacturing landscape [3]. In addition to the more consolidated

✉ Gabriele Piscopo
gabriele.piscopo@polito.it

[1] Department of Management and Production Engineering (DIGEP), Politecnico di Torino, C.so Duca degli Abruzzi, 24, Torino 10129, Italy

Published online: 13 April 2024

sectors such as aerospace, aeronautics and medical, AM applications are emerging in other sectors such as tooling, construction, energy and oil & gas [4].

Considering metal AM processes, the ISO/ASTM 52,900 terminology standard [5] divided the manufacturing systems into three categories that are powder bed, powder deposition and wire deposition systems.

Focusing the attention on the powder deposition system that uses a laser as an energy source, it is possible to refer to this process as Laser Powder Directed Energy Deposition (LP-DED). In this process, a laser beam produces a melt pool on a substrate, and simultaneously powder particles are fed into the molten material by means of a deposition head [6, 7]. The interest in the LP-DED process is growing rapidly and the reasons are in the powerful applications such as repairing operations, production of functionally graded materials and production of large-volume parts [8]. A wide range of metals can be processed by DED [6] however, 316L stainless steel is one of the most interesting in the manufacturing sector if the characteristics of high corrosion resistance, long durability in harsh environments, high hardness, ductility and toughness are needed [9].

However, before using a component produced by the LP-DED process in a functional system, it is mandatory to evaluate the mechanical characteristics of the same component, also in comparison with the ones conventionally produced [10]. According to ISO/ASTM DIS 52,927, tensile strength, hardness and porosity are the most important requirements to be assessed in a part produced by AM processes [11]. Since tensile behavior is one of the most used key performance indicators [12], several efforts were performed to investigate the effect of process parameters [13–15], deposition strategy [16–19] and heat treatment [20, 21] on tensile properties. In general, LP-DED components are characterized by higher tensile properties compared to conventionally manufactured components resulting from the peculiar finer microstructure [22].

For instance, Saboori, et al. [17] showed that LP-DED 316L samples are characterized by a value of Yield Strength (YS) of about 460 MPa, which is much higher than the YS value of 316L parts produced by a conventional casting process (about 260 MPa). However, DED samples exhibit mechanical anisotropy due to the layerwise nature of the process [23]. In detail, Ziętala, et al. [24] showed that the YS and UTS values of 316L samples measured along the building direction are lower than those measured perpendicular to the building direction, due to the presence of interlayer pores.

The microstructure also influences the hardness of the samples. Again, a higher hardness value if compared to conventional processes, was observed in 316L LP-DED samples. Moreover, it was observed that the hardness of the deposited sample could highly vary along the building direction, with higher hardness observed on upper layers [12, 25, 26]. In addition, as evidenced by Chechik, et al. [27] depositing 316L thin walls, the variation of hardness along the building direction highly depends on the material and the process parameters used during the fabrication. Hence, different works analyzed the effect of process parameters. In particular, when low specific energy was used, the hardness values were almost constant or characterized by a slightly increasing trend along the building direction. On the other hand, when the specific energy increased, a significant reduction of hardness along the wall height was observed [27].

Another characteristic to be assessed is the porosity [23]. Depending on the mechanism by which the pores are generated, three categories of pores have been identified in the literature [23, 28]: keyhole pores, gas pores and lack of fusion pores. Keyhole pores arise due to too-high specific energy and are spherical in shape as a result of the vaporization of the material and their size depends on the size of the laser beam [28, 29]. Gas pores are typically small (< 200 μm) and spherical in shape [30, 31] and are mainly caused by gas entrapped inside powder particles during the atomization process or by the entrapment of shielding gas into the melt pool [23, 28, 32]. Finally, the lack of fusion pores, which are usually large and irregular in shape, are caused by insufficient penetration of the melt pool between consecutive tracks and layers [32, 33].

Tan, et al. [34] carried out a characterization of the pore distribution within a 316L sample and showed that, due to the cold substrate, large irregular pores were located in the first layer. Far from the building platform, the pores were small and characterized by an almost spherical shape and this was attributed to moisture evaporation and gas entrapment.

Since a high porosity level facilitates crack propagation, the main objective is to obtain a part with minimum porosity, usually lower than 0.5%, without pores concentration [29]. In fact, pores significantly affect the mechanical properties of the part [6]. For istance, Xue, et al. [35] and Ziętala, et al. [24] showed that both the Yield stress and the Maximum stress decreased with the increase of the porosity level. Similarly, Izadi, et al. [36] observed that also the compressive stiffness decreased increasing the porosity. In general, the reduction of porosity was obtained by adjusting the process parameters [23]. For example, Lin, et al. [37] showed that the porosity of 316L thin wall decreased by increasing the laser power and the travel speed, while it increased with powder feed rate. Subsequently, Piscopo, et al. [38] analyzed the porosity in 316L bulk samples and observed that the lack of fusion pores was reduced by increasing the laser power, but the gas pores increased. An opposite behavior was observed when the powder feed rate was increased. Porosity was also influenced by the laser focus position. In detail, Zheng, et al. [39] showed that interlayer lack of fusion porosities were obtained when close-to-focus settings were used due to the reduction of melt pool dimensions.

Additionally, in LP-DED parts high distortion could arise from the high residual stresses generated by the deposition process [23, 40]. Moreover, it is well-recognized that residual stresses adversely affect the mechanical characteristics of the deposited part. Consequently, several efforts were performed in order to quantify and minimize the residual stresses. Residual stresses are highly non-uniform, with a mean compressive state in the core and a tensile state at the edge [41]. In addition, considering the spatial distribution of residual stresses, the lateral surfaces are characterized by a higher stress level compared to the top surface [20]. All in all, the stresses show an oscillatory distribution [42] and value that can reach 75% of the yield strength [43] with variations gradient up to 100 MPa/mm [23]. The mitigation of residual stresses is fundamental and four different methods are developed and used. These methods are preheating the substrate, optimizing the process parameters, performing heat treatment and optimizing the deposition strategy [44, 45]. It should be noted that although it is universally accepted that preheating the substrate and performing

a heat treatment reduces the residual stress level [23, 46], process parameters cannot be arbitrarily varied since porosity or excessive dilution may occur [47]. Consequently, the optimization of the deposition strategy is the object of most of the works available in the literature. However, most of the works used numerical simulation and are focused on titanium and Inconel alloys. The experimental research on the effect of deposition strategy on residual stresses of 316L samples is very limited. For example, Saboori, et al. [17] investigated the raster deposition strategy with two different rotation angles that are 90° and 67°. They showed that using a rotation of 67° lower residual stresses were obtained.

However, the deposition strategy is defined by different parameters such as the hatching distance, the deposition path and the idle time. However, the time between two consecutive layers, the so-called idle time, is often neglected in the analysis and its evaluation is limited to tensile and microstructure analysis. For example, Yadollahi, et al. [48] showed that idle time influenced the mechanical and microstructural properties of 316L cylindrical samples. In detail, they found that a longer idle time caused a finer microstructure, a higher strength and a lower elongation. Hwang, et al. [49] determined the optimal idle time for 316L thin walls using the constitutive equation and showed that with the optimal idle time a homogeneous grain refinement along the sample height was obtained.

From the analysis of the literature on 316L samples produced by the LP-DED process, it was observed that most of the works investigated the tensile and the microstructural behavior. Porosity and residual stresses are less investigated and the majority of the existing studies analyzed the effect of laser power, travel speed and powder feed rate. However, according to the literature, the deposition strategy that is defined by deposition path, hatching distance and idle time significantly affected the mechanical behavior. Therefore, this work aims to investigate the effect of two deposition strategy parameters, namely the deposition path and the idle time, on the porosity and residual stresses of 316L samples.

Materials and Methods

The experimental procedure adopted in this work is described in the following subsections. Firstly, the system and the material used for sample production are presented. Then, the equipment used for sample characterization in terms of residual stresses and porosity is illustrated.

Samples Production

Several AISI 316L parallelepiped samples with dimensions of $60 \times 15 \times 15$ mm^3 were produced on $110 \times 110 \times 10$ mm^3 substrates of the same material, as illustrated in Fig. 1. 316L gas atomized powder supplied by Oerlikon Metco Inc. (Troy, MI, USA) was used, with a particle size distribution ranging from 45 to 106 μm. The complete characterization of the powder was performed by Vincic [50]. Powder particles were delivered to the deposition area by means of a

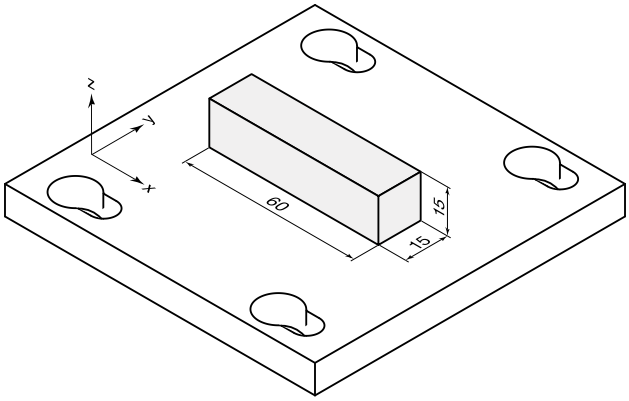

Fig. 1 CAD model of the LP-DED sample

carrier gas. In this work the carrier gas was argon at a pressure of 5 bar and a constant flow of 6 l/min. The same carrier gas is used to create the local shielding atmosphere.

Samples were realized using a LASERDYNE® 430 system developed by Prima Additive (Collegno, Italy). The LASERDYNE® 430 system is equipped with a fiber laser with a maximum laser power of 1000 W. The laser beam has a top hat energy distribution with a diameter of 2 mm in the focal plane.

Focusing on the effect of the deposition strategy on part properties, the production of the samples was carried out by varying the idle time and the deposition path, while keeping other parameters constant. Especially, the laser power, the travel speed and the powder flow rate were set to 650 W, 850 mm/min and 5.5 g/min, respectively, as suggested by the LP-DED system supplier for the 316L powder. The hatching distance that guarantees an overlapping of 50% between adjacent tracks was set up; since the track width is a consequence of energy density and power flow rate, which are invariant in this work, the hatching distance is also considered as a constant parameter. Thus, the third parameter that defines the deposition strategy, which is the hatching distance, was kept constant during all the experiments and set to 1 mm. Given the process parameters and the resulting height of the tracks, a layer thickness of 0.50 mm was set up.

In particular, nine deposition strategies, defined by three deposition paths and three values of idle time, were studied. A standard raster deposition path, with a rotation of 90° at each layer, was analyzed and compared to a raster deposition path with a rotation of 67° at each layer, typically used in Laser Beam Powder Bed Fusion (PBF-LB) systems, and the spiral in-out deposition path, that is widely recognized as being able to generate a more even temperature distribution during deposition [51]. To evaluate the effect of the idle time, depositions with no idle time (0 s) and with increasing values (10 and 20 s) of idle time were investigated. Higher idle times are not of interest from an industrial perspective as they prolong the deposition time to unacceptable values. The samples were coded according to the deposition strategy as reported in Table 1.

Table 1 Sample designation with respect to the deposition strategy parameters used in the experimental procedure

Sample designation	Deposition path	Idle time
	Raster with a rotation of 90° at each layer	
R90_00	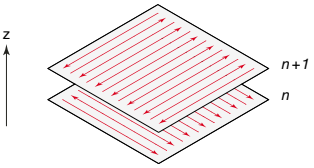	0 s
R90_10		10 s
R90_20		20 s
	Raster with a rotation of 67° at each layer	
R67_00	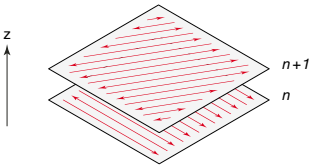	0 s
R67_10		10 s
R67_20		20 s
	Spiral in-out	
SPI_00	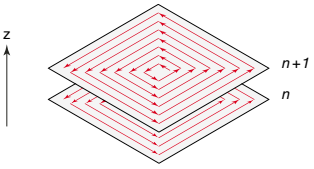	0 s
SPI_10		10 s
SPI_20		20 s

Porosity Evaluation

The porosity of the samples was evaluated through computer tomography (CT) analysis on $10 \times 10 \times 55$ mm^3 coupons extracted from a replica of the samples. In detail, the samples were separated by WEDM at 2.5 mm distance from the substrate and then machined to remove 2.5 mm depth on all the other external surfaces, to keep within the limits of CT scanner and exclude the near-to-surface defects from the analysis. A Phoenix V|tome|x S240 by Baker Hughes (Houston, TX, USA) was used for CT scans, setting a voltage of 210 kV and a current of 110 µA and without the use of any filter in order to achieve the proper balance of sample and background grey values. The acquisition setup led to a voxel size of 20 µm (resolution). For each coupon, 2500 images in a full 360° rotation were acquired. After the acquisition, the raw data were automatically cleaned from possible errors and processed for volume reconstruction using Phoenix datos|x 2 software.

Then, a porosity analysis was performed in the software VGSTUDIO MAX 3.5 by Volume Graphics (Heidelberg, Germany) using the VGDefX algorithm. In detail, the porosity analysis was performed by defining a Region of Interest

(ROI), which is defined as the volume in which the analysis was executed. The definition of the ROI was performed by virtually cutting the entire scanned volume of the sample using the clipping box function available in the software. The ROI was characterized by dimensions of about $10 \times 10 \times 15$ mm^3, including the end of the coupon and an intermediate volume. In this way, it was possible to analyze the porosities on both the edge of the sample, where a temperature accumulation is typically observed due to lower heat exchange and path inversion, and the core of the sample, where a more regular behavior is expected. Porosities were then determined in the defined ROI by comparing the grey value deviation between two adjacent voxels using a contrast level of about 3500 and a probability threshold of 0.70. According to the voxel resolution, only pores with a diameter larger than 40 µm (limited by 2 times the CT scan voxel size) were considered in the analysis.

Residual Stresses

The hole-drilling strain gauge method was selected to investigate residual stresses beneath the surface according to the ASTM E837-20 standard [52]. The residual stress distribution was measured on the top surface of each sample, as illustrated in Fig. 2, after surface cleaning and smoothing in the measurement area to improve the strain-gauge adhesion. The surface preparation was manually performed using abrasive SiC paper with different grain dimensions (220, 400 and 600 grit). The procedure used for surface preparation and rosette gluing is detailed in [20]. Stresses were measured before detaching the samples from the substrate in order to measure the stress induced by the mere production process and avoid the stress relaxation due to the separation operation. The Restan MTS300 system (SINT Technology S.r.l, Italy), equipped with an inverted cone drill bit characterized by a diameter of 1.6 mm, was used to produce a 1.2 mm deep flat-bottom hole. In detail, the hole was obtained through a sequence of 24 drill steps of 50 µm each. Each drilling step caused material removal and therefore, a stress redistribution and deformation of the

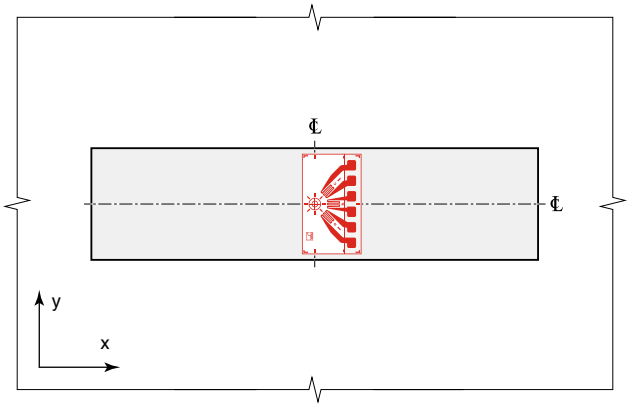

Fig. 2 Position of the strain gage rosette on the top surface of the LP-DED sample

material. The deformations were measured by K-RY61-1.5/120R (HBM Italia S.r.l., Italy) Type B 3-element rosette connected to an amplifier and acquired by the automatic RSM software. In detail, the QuantumX MX440B amplifier (HBK GmbH, Germany) was used. This amplifier was characterized by 4 channels, a resolution of 24 bits, and a sampling rate of 40 kHz. The RSM software (HBM Italia S.r.l., Italy) was used to control the whole acquisition process and to save the measured deformations.

The acquired deformations were then elaborated using the EVAL software (SINT Technology S.r.l, Italy) in order to compute the residual stresses along the analyzed depth according to ASTM E837-20 standard.

Results and Discussion

All the samples were successfully produced without any visible surface defects. Figure 3 shows a replica of the samples produced with the three different deposition paths and no idle time. From a preliminary visual inspection of the samples produced, the effect of the deposition path on the external morphology of the top surface of the sample was clear. The influence of the deposition path on the thermal history was also evident from the different colors of the oxides on the external surfaces. In particular, as observed by Vecchi, et al. [53], higher temperatures were expected when the oxides tended to dark blue colors.

Porosity

The porosity analysis in VGSTUDIO MAX allowed to detect and visualize the spatial distribution of the pores, to characterize their shape and size, and to determine global parameters such as total porosity in the analyzed volume. Results showed that the porosity of the samples produced with the standard deposition strategy, that is a raster path rotating 90° at each layer, was 0.21% without idle time and increased to 0.35% at the highest idle time. Nevertheless, all these samples satisfied the limit suggested by Svetlizky, et al. [23] of the maximum porosity level of 0.50%. The

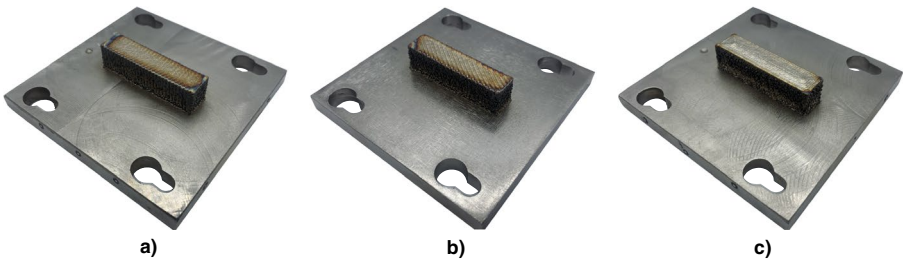

Fig. 3 316L samples produced with no idle time and with different deposition paths: **a** raster with a rotation of 90° at each layer, **b** raster with a rotation of 67° at each layer, and (**c**) spiral in-out

adoption of the 67° rotation of the raster deposition path led to lower values of porosity, between 0.13% without idle time and 0.26% with 20 s of idle time. This was attributed to a more homogenous temperature distribution and the uniform melt pool formation caused by the lower cyclicity during the production of the samples [54]. This aspect was also observed in PBF-LB processes where the use of a 67° rotation angle led to a more random distribution of the temperature and of the melt pool [55–57]. The spiral deposition path caused an increased total porosity, ranging from 0.35 to 0.60%. All the results are listed in Table 2. The high porosity detected in the sample SPI_20 realized with the spiral deposition path and 20 s of idle time, that was higher with respect to the maximum porosity value recommended by [29], suggests that this deposition strategy should be rejected, at least with the adopted process parameters. Based on these results, is thus possible to state that the deposition path and the idle time significantly affected the total porosity. In particular, it was also possible to observe that for all the deposition paths analyzed in this work, increasing the idle time value caused an increase in the porosity value. This behavior could be explained by considering that as the idle time increased, the temperature of the deposited material progressively decreased [58]. Therefore, with all other process parameters held constant, the thermal energy provided to the material was insufficient to produce a stable melt pool as the temperature gap increased.

The porosity distributions within the samples produced with the three deposition paths and idle times are illustrated in Fig. 4. The spatial distribution of porosity changed significantly with the deposition path and pores were mainly located at the interface between layers, in some cases hinting at the path itself. This is particularly evident in the sample produced by the spiral deposition path, where all the tracks in the layer were aligned with those of the previous layer and intertrack porosity developed.

From the pore size distribution, illustrated in Fig. 5, it was possible to observe that most pores had a diameter lower than 0.2 mm. Furthermore, these pores were also characterized by a high value of sphericity and consequently, they were identified as gas-entrapped pores. Very few pores were characterized by a diameter larger than 0.6 mm and a low value of sphericity, and these pores were classified as lack of fusion pores.

Table 2 Porosity level measured on the analyzed samples

Deposition path	Sample	Total porosity
Raster with a rotation of 90° at each layer and no idle time	R90_00	0.21%
Raster with a rotation of 90° at each layer and 10 s idle time	R90_10	0.26%
Raster with a rotation of 90° at each layer and 20 s idle time	R90_20	0.35%
Raster with a rotation of 67° at each layer and no idle time	R67_00	0.13%
Raster with a rotation of 90° at each layer and 10 s idle time	R67_10	0.19%
Raster with a rotation of 90° at each layer and 20 s idle time	R67_20	0.26%
Spiral in-out and no idle time	SPI_00	0.35%
Spiral in-out and 10 s idle time	SPI_10	0.48%
Spiral in-out and 20 s idle time	SPI_20	0.60%

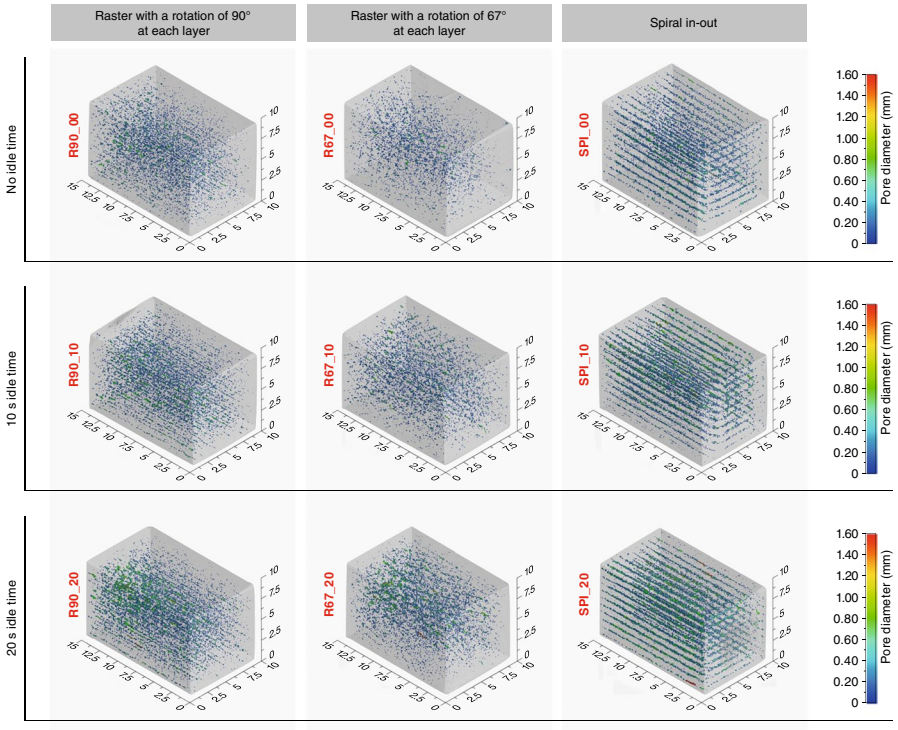

Fig. 4 Spatial distribution of porosity measured in the sample produced with different deposition paths and times

Comparing the results in Fig. 5, it is possible to observe that the increase in the idle time caused an increase in the number of lack of fusion pores and in their diameter. In details, a larger number of lack of fusion pores was observed in samples produced with 20 s of idle time, with a higher percentage when the deposition path was in-out spiral. The maximum pore diameter measured in SPI_20 sample was 1.58 mm.

Overall, it was observed that both the deposition path and the idle time influenced the porosities measured in the samples. Specifically, these parameters mostly influenced the amount and the dimension of the lack of fusion pores, while gas-entrapped pores were almost constant and equal to 0.10% in all the analyzed samples. The porosity related to gas entrapped pores may be attributed to the carrier gas flow rate or the initial condition of the powder, in terms of relative humidity and inherent porosity [23, 28, 59]. Since the carrier gas flow rate did not change in the experiments, and the same powder batch was used in the deposition tests, the constancy of gas-entrapment resulting porosity is justified.

Combining Figs. 4 and 5, it can be observed that the pores with a diameter lower than 0.2 mm were uniformly distributed along the building direction in the ROI considered, even if in some cases the deposition path in the layer is understandable,

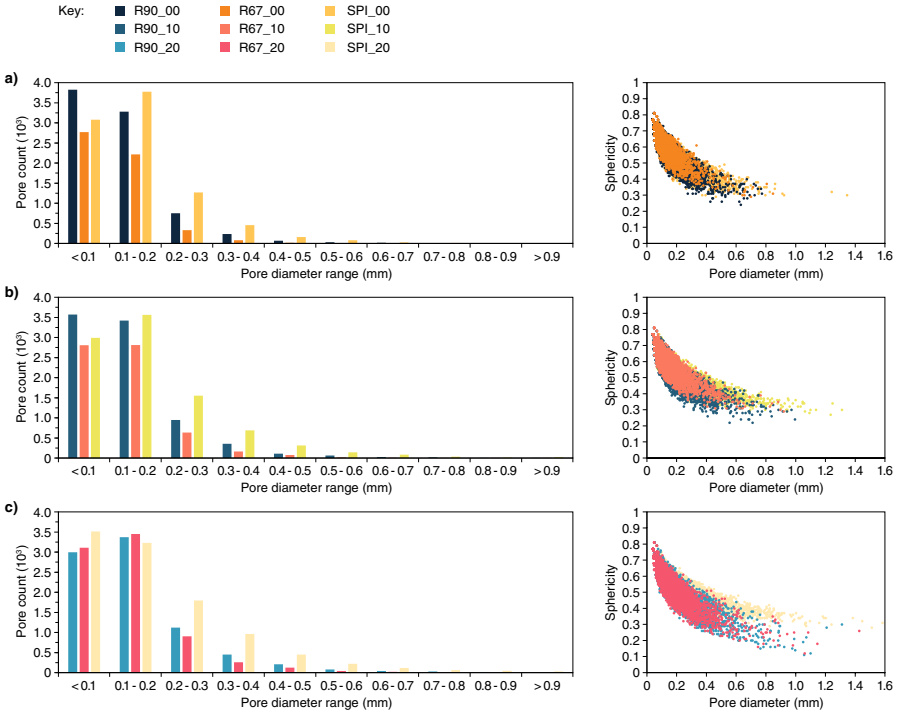

Fig. 5 Distribution of pore sizes within the samples and relation between sphericity and pore diameter of samples produced with (**a**) 0 s, (**b**) 10 s and (**c**) 20 s values of idle time

confirming the intrinsic nature of these pores. On the other hand, the pores with a large diameter, greater than 0.6 mm, were mainly located in the lower part of each sample, where the mean temperature of the deposit was lower. In fact, during the process the mean temperature of the deposit tends to increase do to heat accumulation. Consequently, the specific energy required to obtain a proper dilution between layer and hence a reduction of lack-of-fusion pores, decreased with the deposit height confirming the finding of [34] and [38].

Therefore, the differences observed in the lack-of-fusion porosity of the samples can be explained by considering the temperature distributions induced by the different deposition paths. The spiral distribution path was adopted in the experimental design since it was demonstrated by Yu, et al. [51] to be able to generate a nearly symmetric temperature distribution at the end of the deposition process and almost constant temperature gradients during building. However, with respect to the raster deposition path, inevitably involved a lower temperature in preceding layers hence an higher temperature gradient between two consecutive layers Yu, et al. [51], thus preventing proper dilution of tracks during the deposition of subsequent layers.

Summarizing the results, it was observed that, despite for all the deposition paths lack-of-fusion pores were observed, the deposition path can be used to minimize the temperature gradient and reduce lack-of-fusion pores. However, without the

selection of the process parameters to obtain a proper value of specific energy, it is not enough.

Similarly, it is possible to explain the effect of idle time. In fact, as the idle time increases, the overall temperature of the sample decreases. The lower temperature may be compensated with an increase in specific energy, but this approach is undesired when the goal is to minimize the thermal stresses and the substrate alteration. Another possibility is to reduce the layer thickness, resulting in a lower productivity. Further studies should consider variants of the spiral deposition path, including segmentation options and path shifting at each layer.

Residual Stresses

Figure 6 shows the residual stress distribution (σ_{max} and σ_{min}) and direction of the maximum principal stress (β) measured on the different samples. It is possible to observe that the lowest residual stresses in the depth were measured in the sample R90_00, built with the standard deposition path. In this sample, an initial

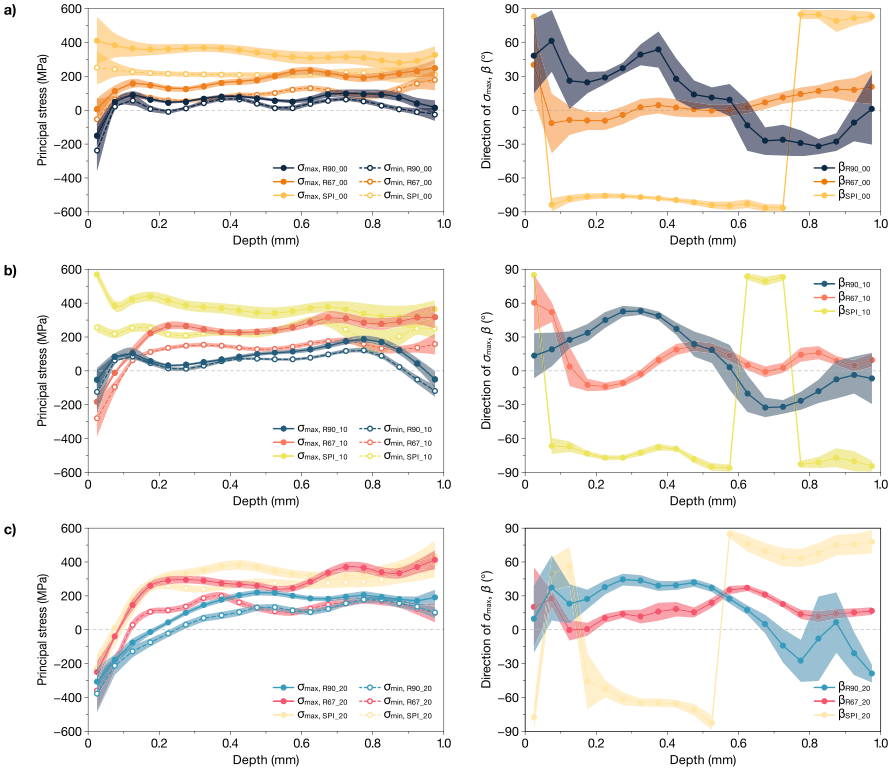

Fig. 6 Residual stress distribution measured on the top surface of the samples with (**a**) no idle time, (**b**) 10 s idle time and (**c**) 20 s idle time

compressive stress state was observed with the value of maximum principal stress of -150 MPa. Then, the stress sharply increased and a local maximum value of 93 MPa was observed at a depth of 0.125 mm. After this depth, the maximum principal stress oscillated between 52 MPa and 95 MPa. It is worth noting that the adopted process parameters, namely laser power and travel speed, combined with the 90° deposition strategy, are optimized for the 316L material to best balance between porosity and residual stresses. Thus, this behavior of the R90_00 sample was expected and confirmed the process reliability. In the sample R67_00, which exhibited to lowest porosity, the measured stresses showed a trend very similar to that observed in sample R90_00, but the stress values were moderately higher confirming the finding of [17]. In fact, the initial value of the maximum principal stress was of about 10 MPa and then it increased, reaching the maximum value of about 240 MPa at a depth of about 0.6 mm. Higher residual stresses were measured on sample SPI_00, with a nearly uniform stress profile along the depth, with a maximum stress of about 350 MPa. This result is consistent with the more uniform temperature distribution obtained with the spiral deposition strategy Yu, et al. [51, 53], combined with the lower temperatures in preceding layers that caused higher thermal stresses, given the same energy density in all the experiments.

Analyzing the direction of the maximum principal stress, the β value measured on the sample R90_00 ranged between 60° and −30°. Combining this result with the orientation of the strain gauge rosette installed on the top surface of the sample gives a principal stress direction of approximately 15° from the longitudinal axis of the sample. The β angle measured in the R67_00 sample is quite constant along all the analyzed depth, with a 0° mean value and a variance of ±15°. This outcome was attributed to the strategy of rotating the deposition path at each layer to avoid aligning the tracks in successive layers. In this sample, the direction of the principal stress is thud about 45° from the longitudinal axis. The value of β measured in the sample SPI_00 was of about 90°, meaning that the maximum principal stress is directed at 45° from the longitudinal axis.

The residual distribution and the direction of the maximum principal stress of samples produced with 10 and 20 s idle times are shown in Fig. 6b and c. At 10 s of idle time, the stress trend was similar to that observed in the samples produced with no idle time. In fact, similarly to the latter, higher stresses were observed in the sample produced with the spiral deposition path, and the lower stresses were measured in the sample produced using the raster deposition path with 90° rotations. More in detail, comparing the residual stresses depicted in Fig. 6a and b, it is possible to observe that no significant differences were measured between the samples SPI_00 and SPI_10. Conversely, in the other samples, the increase in idle time from 0 to 10 s caused an increase in residual stresses of about 50 MPa, which is particularly evident after a depth of 0.5 mm, corresponding to the penultimate layer. Analyzing the direction of the maximum principal stress it was possible to observe that no significant variations were obtained between the samples produced with an idle time of 10 s and samples produced without idle time.

In the case of 20 s idle time, it is possible to observe that the differences in residual stress are narrowing, mainly because the stresses generated in the samples with raster deposition paths increased at values closer to those observed

in the spiral sample. In detail, all the samples showed a subsurface compressive stress with the maximum principal stress ranging between − 227 MPa and − 306 MPa, and the higher compressive stress was measured on sample R90_20. In addition, for a depth greater than 0.3 mm, no significant differences were observed between samples produced respectively using 10 and 20 s idle times. Then, analyzing the maximum principal stress direction, it was noticed that the idle time had only a slight influence on the β value, more visible on the R67_20 sample.

Summarizing the results depicted in Fig. 6, it was observed that both the deposition path and the idle time influenced the residual stress distribution measured in the produced samples. In particular, the different residual stress distributions observed by varying the deposition path could be attributed to the different temperature distributions induced in the samples. In fact, as observed by Yu, et al. [51] the spiral deposition strategy induces a lower mean temperature in the sample during the deposition process, and consequently a higher temperature gradient between two consecutive layers. On the other hand, based on the distribution of residual stresses, it is possible to state that the higher temperature was obtained when a raster deposition path strategy with a rotation of 90° at each layer was used and this result confirmed the findings of [51]. Then, it was observed that an increase in idle time generally led to an increase in the residual stress value. This is particularly evident when the idle time is increased from 0 to 10 s for samples produced using raster deposition strategies. In fact, as the idle time increased, the temperature decreased and consequently the residual stresses, which are proportional to the temperature gradient, were higher. In addition, results highlight that the deposition path had a strong influence on the direction of the maximum principal stress (β), on the contrary the β value was only slightly influenced by the idle time.

Conclusion

In this work, the effect of two parameters of the motion path, that are the deposition path and the idle time, on the porosity and the residual stresses of 316L samples produced by the LP-DED process is investigated. All the samples were successfully produced and were free from evident defects.

The results showed that:

- The porosity in the produced samples ranged between 0.13% and 0.60% and this value was strongly influenced by the deposition strategy parameters investigated in the current work. Specifically, the lower porosity value was obtained in the sample produced with a raster deposition path rotated 67° at each layer and without the use of an idle time.
- The residual stress value ranged from − 400 MPa to 400 MPa in all the samples. The value depended significantly on the deposition path used with the higher values obtained when the spiral deposition path was used. On the other hand, the effect of idle time must be related to the deposition path used. In fact, when

the spiral deposition path was used, the stresses were almost independent of the idle time, whereas when the raster deposition paths were used, an increase in idle time caused an increase in residual stresses.
- The direction of the maximum principal stress was influenced by the deposition path but not by the idle time.

Acknowledgements The authors would like to thank Prof. Eleonora Atzeni and Prof. Alessandro Salmi for their precious help and support in this research. We also acknowledge the resources of the Interdepartmental Centre for Integrated Additive Manufacturing (IAM@PoliTo) at the Politecnico di Torino, Turin, Italy.

Author Contributions G.P. and L.I. wrote the manuscript text, G.P. and L.I. Conceptualization, G.P. sample production, G.P. and L.I. experimental investigation and results interpretation.

Funding Open access funding provided by Politecnico di Torino within the CRUI-CARE Agreement.

Data Availability Not applicable.

Declarations

The authors have no relevant financial or non-financial interests to disclose.

Competing Interests The authors declare no competing interests.

Ethical Approval Not applicable.

References

1. Thompson, M.K., Moroni, G., Vaneker, T., Fadel, G., Campbell, R.I., Gibson, I., Bernard, A., Schulz, J., Graf, P., Ahuja, B., Martina, F.: Design for Additive Manufacturing: Trends, opportunities, considerations, and constraints. CIRP Ann. **65**(2):737–760. https://doi.org/10.1016/j.cirp.2016.05.004
2. Madhavadas, V., Srivastava, D., Chadha, U., Aravind Raj, S., Sultan, M.T.H., Shahar, F.S., Shah, A.U.M.: A review on metal additive manufacturing for intricately shaped aerospace components. CIRP J. Manufact. Sci. Technol. **39**:18–36. https://doi.org/10.1016/j.cirpj.2022.07.005
3. Stavropoulos, P., Foteinopoulos, P., Stavridis, J., Bikas, H.: Increasing the industrial uptake of additive manufacturing processes: A training framework. Adv. Ind. Manuf. Eng. **6**. https://doi.org/10.1016/j.aime.2022.100110
4. Wohlers, T., Caffrey, T., Campbell, R.I., Diegel, O., Kowen, J.: Wohlers Report 2022: 3D Printing and Additive Manufacturing State of the Industry; Annual Worldwide Progress Report. Wohlers Associates (2022)

5. International, A.S.T.M.: ISO/ASTM 52900:2021(E) - Standard Terminology for Additive Manufacturing – General Principles – Terminology. ASTM International (2021)
6. Gibson, I., Rosen, D., Stucker, B.: Directed Energy deposition processes. In: Additive Manufacturing Technologies, 2nd edn., pp. 245–268. Springer, New York (2015). https://doi.org/10.1007/978-1-4939-2113-3_10
7. Piscopo, G., Salmi, A., Atzeni, E.: Investigation of dimensional and geometrical tolerances of laser powder directed energy deposition process. Precis. Eng. **85** :217–225. https://doi.org/10.1016/j.precisioneng.2023.10.006
8. Piscopo, G., Iuliano, L.: Current research and industrial application of laser powder directed energy deposition. Int. J. Adv. Manuf. Tech. **119**(11–12):6893–6917. https://doi.org/10.1007/s00170-021-08596-w
9. Shrinivas Mahale, R., Shamanth, V., Hemanth, K., Nithin, S.K., Sharath, P.C., Shashanka, R., Patil, A., Shetty, D.: Processes and applications of metal additive manufacturing. Mater. Today: Proc. **54**:228–233. https://doi.org/10.1016/j.matpr.2021.08.298
10. Azarniya, A., Colera, X.G., Mirzaali, M.J., Sovizi, S., Bartolomeu, F., St Weglowski, M., Wits, W.W., Yap, C.Y., Ahn, J., Miranda, G., Silva, F.S., Madaah Hosseini, H.R., Ramakrishna, S., Zadpoor, A.A.: Additive manufacturing of Ti–6Al–4V parts through laser metal deposition (LMD): Process, microstructure, and mechanical properties. J. Alloy Compd. **804**:163–191. https://doi.org/10.1016/j.jallcom.2019.04.255
11. ISO. ISO/ASTM DIS 52927 Additive manufacturing — General principles — Main Characteristics and Corresponding test Methods, ISO/ASTM
12. Saboori, A., Aversa, A., Marchese, G., Biamino, S., Lombardi, M., Fino, P.: Microstructure and mechanical properties of AISI 316L produced by directed energy deposition-based additive manufacturing: A review. Appl. Sci. (Switzerland) **10**(9). https://doi.org/10.3390/app10093310
13. Wang, Z., Palmer, T.A., Beese, A.M.: Effect of processing parameters on microstructure and tensile properties of austenitic stainless steel 304L made by directed energy deposition additive manufacturing. Acta Mater. **110**:226–235. https://doi.org/10.1016/j.actamat.2016.03.019
14. Aversa, A., Marchese, G., Bassini, E.: Directed energy deposition of aisi 316l stainless steel powder: Effect of process parameters. Metals-Basel **11**(6). https://doi.org/10.3390/met11060932
15. Era, I.Z., Liu, Z.: Effect of process parameters on tensile properties of SS 316 prepared by directional energy deposition. Procedia CIRP **103**:115–121. https://doi.org/10.1016/j.procir.2021.10.018
16. Zhi'En, T., Pang, E., Kaminski, J.H.L.: J.: Directed energy deposition build process control effects on microstructure and tensile failure behaviour. J. Mater. Process. Tech. **294**. https://doi.org/10.1016/j.jmatprotec.2021.117139
17. Saboori, A., Piscopo, G., Lai, M., Salmi, A., Biamino, S.: An investigation on the effect of deposition pattern on the microstructure, mechanical properties and residual stress of 316L produced by Directed Energy Deposition. Mat. Sci. Eng. Struct. **780**. https://doi.org/10.1016/j.msea.2020.139179
18. Wang, X., Deng, D., Qi, M., Zhang, H.: Influences of deposition strategies and oblique angle on properties of AISI316L stainless steel oblique thin-walled part by direct laser fabrication. Opt. Laser Technol. **80**, 138–144 (2016). https://doi.org/10.1016/j.optlastec.2016.01.002
19. Li, J., Deng, D., Hou, X., Wang, X., Ma, G., Wu, D., Zhang, G.: Microstructure and performance optimisation of stainless steel formed by laser additive manufacturing. Mater. Sci. Technol. **32**(12):1223–1230. https://doi.org/10.1080/02670836.2015.1114774
20. Aversa, A., Piscopo, G., Salmi, A., Lombardi, M.: Effect of heat treatments on residual stress and properties of AISI 316L steel processed by directed energy deposition. J. Mater. Eng. Perform. **29**(9):6002–6013. https://doi.org/10.1007/s11665-020-05061-9
21. Nath, P., Nanda, D., Dinda, G.P., Sen, I.: Assessment of microstructural evolution and mechanical properties of laser metal deposited 316L stainless steel. J. Mater. Eng. Perform. **30**(9):6996–7006. https://doi.org/10.1007/s11665-021-06101-8
22. Li, S.-H., Kumar, P., Chandra, S., Ramamurty, U.: Directed energy deposition of metals: Processing, microstructures, and mechanical properties. Int. Mater. Rev. 1–43. https://doi.org/10.1080/09506608.2022.2097411
23. Svetlizky, D., Das, M., Zheng, B., Vyatskikh, A.L., Bose, S., Bandyopadhyay, A., Schoenung, J.M., Lavernia, E.J., Eliaz, N.: Directed energy deposition (DED) additive manufacturing: Physical characteristics, defects, challenges and applications. Mater. Today **49**:271–295. https://doi.org/10.1016/j.mattod.2021.03.020
24. Ziętala, M., Durejko, T., Polański, M., Kunce, I., Płociński, T., Zieliński, W., Łazińska, M., Stępniowski, W., Czujko, T., Kurzydłowski, K.J., Bojar, Z.: The microstructure, mechanical

properties and corrosion resistance of 316L stainless steel fabricated using laser engineered net shaping. Mater. Sci. Eng.: A **677**:1–10. https://doi.org/10.1016/j.msea.2016.09.028
25. El Kadiri, H., Wang, L., Horstemeyer, M.F., Yassar, R.S., Berry, J.T., Felicelli, S., Wang, P.T.: Phase transformations in low-alloy steel laser deposits. Mater. Sci. Eng.: A **494**(1–2):10–20. https://doi.org/10.1016/j.msea.2007.12.011
26. Sun, G.F., Shen, X.T., Wang, Z.D., Zhan, M.J., Yao, S., Zhou, R., Ni, Z.H.: Laser metal deposition as repair technology for 316L stainless steel: Influence of feeding powder compositions on microstructure and mechanical properties. Opt. Laser Technol. **109**:71–83. https://doi.org/10.1016/j.optlastec.2018.07.051
27. Chechik, L., Boone, N.A., Stanger, L.R., Honniball, P., Freeman, F., Baxter, G., Willmott, J.R., Todd, I.: Variation of texture anisotropy and hardness with build parameters and wall height in directed-energy-deposited 316L steel. Addit. Manuf. **38**. https://doi.org/10.1016/j.addma.2020.101806
28. DebRoy, T., Wei, H.L., Zuback, J.S., Mukherjee, T., Elmer, J.W., Milewski, J.O., Beese, A.M., Wilson-Heid, A., De, A., Zhang, W.: Additive manufacturing of metallic components – process, structure and properties. Prog. Mater. Sci. **92**:112–224. https://doi.org/10.1016/j.pmatsci.2017.10.001
29. Herzog, D., Seyda, V., Wycisk, E., Emmelmann, C.: Additive manufacturing of metals. Acta Mater. **117**:371–392. https://doi.org/10.1016/j.actamat.2016.07.019
30. Sinclair, L., Leung, C.L.A., Marussi, S., Clark, S.J., Chen, Y., Olbinado, M.P., Rack, A., Gardy, J., Baxter, G.J., Lee, P.D.: In situ radiographic and ex situ tomographic analysis of pore interactions during multilayer builds in laser powder bed fusion. Addit. Manuf. **36**. https://doi.org/10.1016/j.addma.2020.101512
31. Sohn, H., Liu, P., Yoon, H., Yi, K., Yang, L., Kim, S.: Real-time porosity reduction during metal directed energy deposition using a pulse laser. J. Mater. Sci. Technol. **116**:214–223. https://doi.org/10.1016/j.jmst.2021.12.013
32. Sames, W.J., List, F.A., Pannala, S., Dehoff, R.R., Babu, S.S.: The metallurgy and processing science of metal additive manufacturing. Int. Mater. Rev. **61**(5):315–360. https://doi.org/10.1080/09506608.2015.1116649
33. Kan, W.H., Chiu, L.N.S., Lim, C.V.S., Zhu, Y., Tian, Y., Jiang, D., Huang, A.: A critical review on the effects of process-induced porosity on the mechanical properties of alloys fabricated by laser powder bed fusion. J. Mater. Sci. **57**(21):9818–9865. https://doi.org/10.1007/s10853-022-06990-7
34. Tan, Z.E.E., Pang, J.H.L., Kaminski, J., Pepin, H.: Characterisation of porosity, density, and microstructure of directed energy deposited stainless steel AISI 316L. Addit. Manuf. **25**:286–296. https://doi.org/10.1016/j.addma.2018.11.014
35. Xue, Y., Pascu, A., Horstemeyer, M.F., Wang, L., Wang, P.T.: Microporosity effects on cyclic plasticity and fatigue of LENS™-processed steel. Acta Mater. **58**(11):4029–4038. https://doi.org/10.1016/j.actamat.2010.03.014
36. Izadi M., Farzaneh A., Gibson I., Rolfe B.: The effect of process parameters and mechanical properties of direct energy deposited stainless steel 316. 2017 International Solid Freeform Fabrication Symposium, 2017, University of Texas at Austin. https://ris.utwente.nl/ws/files/252838946/TheEffectofProcessParametersandMechanicalPr.pdf
37. Lin, P.-Y., Shen, F.-C., Wu, K.-T., Hwang, S.-J., Lee, H.-H.: Process optimization for directed energy deposition of SS316L components. Int. J. Adv. Manuf. Technol. **111**(5–6):1387–1400. https://doi.org/10.1007/s00170-020-06113-z
38. Piscopo, G., Atzeni, E., Iuliano, L., Salmi, A.: Tuning Process Parameters to Control the Porosity of Parts Produced with Directed Energy Deposition. In: Flexible Automation and Intelligent Manufacturing: Establishing Bridges for More Sustainable Manufacturing Systemsedn. 434–443 (2024)
39. Zheng, B., Haley, J.C., Yang, N., Yee, J., Terrassa, K.W., Zhou, Y., Lavernia, E.J., Schoenung, J.M.: On the evolution of microstructure and defect control in 316L SS components fabricated via directed energy deposition. Mater. Sci. Eng. A **764**, 138243 (2019). https://doi.org/10.1016/j.msea.2019.138243
40. Izadi, M., Farzaneh, A., Mohammed, M., Gibson, I., Rolfe, B.: A review of laser engineered net shaping (LENS) build and process parameters of metallic parts. Rapid Prototyp. J. **26**(6):1059–1078. https://doi.org/10.1108/Rpj-04-2018-0088
41. Rangaswamy, P., Holden, T.M., Rogge, R.B., Griffith, M.L.: Residual stresses in components formed by the laserengineered net shaping (LENS®) process. J. Strain Anal. Eng. Des. **38**(6):519–527. https://doi.org/10.1243/030932403770735881

42. Strantza, M., Vrancken, B., Prime, M.B., Truman, C.E., Rombouts, M., Brown, D.W., Guillaume, P., Van Hemelrijck, D.: Directional and oscillating residual stress on the mesoscale in additively manufactured Ti-6Al-4V. Acta Mater. **168**:299–308. https://doi.org/10.1016/j.actamat.2019.01.050
43. Rangaswamy, P., Griffith, M.L., Prime, M.B., Holden, T.M., Rogge, R.B., Edwards, J.M., Sebring, R.J.: Residual stresses in LENS® components using neutron diffraction and contour method. Mater. Sci. Eng.: A **399**(1–2):72–83. https://doi.org/10.1016/j.msea.2005.02.019
44. Ahn, D.-G.: Directed Energy Deposition (DED) process: State of the art. Int. J. Precis Eng. Manuf. - Green. Technol. **8**(2):703–742. https://doi.org/10.1007/s40684-020-00302-7
45. Piscopo, G., Atzeni, E., Saboori, A., Salmi, A.: An overview of the process mechanisms in the laser Powder Directed Energy Deposition. Appl. Sci. (Switzerland) **13**(1). https://doi.org/10.3390/app13010117
46. Vasinonta, A., Beuth, J.L., Griffith, M.: Process maps for Predicting residual stress and Melt Pool size in the laser-based fabrication of thin-walled structures. J. Manuf. Sci. Eng. **129**(1):101–109. https://doi.org/10.1115/1.2335852
47. Dass, A., Moridi, A.: State of the art in directed energy deposition: from additive manufacturing to materials design. Coatings **9**(7). https://doi.org/10.3390/coatings9070418
48. Yadollahi, A., Shamsaei, N., Thompson, S.M., Seely, D.W.: Effects of process time interval and heat treatment on the mechanical and microstructural properties of direct laser deposited 316L stainless steel. Mater. Sci. Eng.: A **644**:171–183. https://doi.org/10.1016/j.msea.2015.07.056
49. Hwang, S., Oh, W.-J., Kim, D.-H., Kim, J.G., Oh, J.S., Nam, T.-H., Kim, C.-S., Lee, T.: Optimizing interlayer cooling for SUS316L thin wall fabricated by directed energy deposition. J. Mater. Res. Technol. **23**:5239–5245. https://doi.org/10.1016/j.jmrt.2023.02.145
50. Vincic, J.: Laser Directed Energy Deposition for Processing and Repairing Steels PhD Thesis, Politecnico di Torino, (2024)
51. Yu, J., Lin, X., Ma, L., Wang, J., Fu, X., Chen, J., Huang, W.: Influence of laser deposition patterns on part distortion, interior quality and mechanical properties by laser solid forming (LSF). Mater. Sci. Eng.: A **528**(3):1094–1104. https://doi.org/10.1016/j.msea.2010.09.078
52. International, A.S.T.M.: Standard Test Method for Determining Residual Stresses by the Hole-drilling Strain-gage Method. ASTM International (2020)
53. Vecchi, G., Atzeni, E., Iuliano, L., Salmi, A.: Control of the Substrate Heating in Laser Powder Directed Energy Deposition Repairing by Bi-Directional Spiral Deposition Strategy. Euro PM2023 Proceedingsed. 2023. https://doi.org/10.59499/EP235762610
54. Mishra, G.K., Paul, C.P., Rai, A.K., Agrawal, A.K., Rai, S.K., Bindra, K.S.: Experimental investigation on Laser Directed Energy Deposition based additive manufacturing of Al2O3 bulk structures. Ceram. Int. **47**(4):5708–5720. https://doi.org/10.1016/j.ceramint.2020.10.157
55. Zhang, X., Xu, H., Li, Z., Dong, A., Du, D., Lei, L., Zhang, G., Wang, D., Zhu, G., Sun, B.: Effect of the scanning strategy on microstructure and mechanical anisotropy of Hastelloy X superalloy produced by Laser Powder Bed Fusion. Mater. Charact. **173**. https://doi.org/10.1016/j.matchar.2021.110951
56. Leicht, A., Yu, C.H., Luzin, V., Klement, U., Hryha, E.: Effect of scan rotation on the microstructure development and mechanical properties of 316L parts produced by laser powder bed fusion. Mater. Charact. **163**. https://doi.org/10.1016/j.matchar.2020.110309
57. Marattukalam, J.J., Karlsson, D., Pacheco, V., Beran, P., Wiklund, U., Jansson, U., Hjörvarsson, B., Sahlberg, M.: The effect of laser scanning strategies on texture, mechanical properties, and site-specific grain orientation in selective laser melted 316L SS. Mater. Des. **193**. https://doi.org/10.1016/j.matdes.2020.108852
58. Chua, B.-L., Ahn, D.-G.: Estimation method of interpass time for the control of temperature during a directed energy deposition process of a Ti–6Al–4V Planar Layer. Materials **13**(21). https://doi.org/10.3390/ma13214935
59. Wolff, S.J., Wang, H., Gould, B., Parab, N., Wu, Z., Zhao, C., Greco, A., Sun, T.: In situ X-ray imaging of pore formation mechanisms and dynamics in laser powder-blown directed energy deposition additive manufacturing. Int. J. Mach. Tools Manuf. **166**. https://doi.org/10.1016/j.ijmachtools.2021.103743